JUNO 水相中太阳中微子信号寻找

The search for solar neutrino signals in the JUNO water phase

(申请清华大学理学博士学位论文)

培 养 单 位： 工程物理系

学　　　科： 物理学

研 究 生： 翁　　俊

指 导 教 师： 郑 纬 民　 教　授

副指导教师： 陈 文 光　 教　授

二〇二五年八月

The search for solar neutrino signals in the JUNO water phase

Dissertation submitted to

Tsinghua University

in partial fulfillment of the requirement

for the degree of

Doctor of Philosophy

in

Physics

by

Weng Jun

Dissertation Supervisor : Professor Zheng Weimin

Associate Supervisor : Professor Chen Wenguang

August, 2025

TABLE OF CONTENTS

CHAPTER 1 INTRODUCTION

CHAPTER 2 THE JUNO DETECTOR

The Jiangmen Underground Neutrino Observatory (JUNO) is a multipurpose neutrino experiment under construction in southern China. The primary scientific objective of JUNO is to determine the neutrino mass ordering and precisely measure neutrino oscillation parameters by detecting reactor antineutrinos from the Yangjiang and Taishan nuclear power plants, located approximately 53 km from the JUNO site. The JUNO detector consists of a central detector (CD) containing 20 kilotons of liquid scintillator (LS), a water Cherenkov detector (WCD) serving as a cosmic muon veto, and a top tracker (TT) for additional muon tracking. The CD is housed within a large acrylic sphere with a diameter of 35.4 m, which is further enclosed by a stainless steel lattice structure. The WCD surrounds the CD and is filled with 35 kilotons of ultrapure water, while the TT is positioned above the WCD. The entire detector assembly is situated approximately 700 m underground, equivalent to 1800 m of water overburden, to mitigate cosmic ray interference.

CHAPTER 3 THE PMT CALIBRATION IN WATER PHASE

3.1 The single electron response of MCP-PMTs

The photomultiplier tubes (PMT) see extensive deployments in particle physics, particularly neutrino experiments. A PMT comprises a photocathode, an electron multiplier, an anode, and other necessary structural components[1]. Photons from a light source incident on the photocathode follow a Poisson process. Some of them are converted to photoelectrons (PE) via the photoelectric effect and such PEs enter the multiplier[2]. Those two processes are Bernoulli selections, with the probabilities known as the *quantum efficiency* (QE) and the *collection efficiency* (CE). The PE count (n_{PE}) in a specific time interval follows a Poisson distribution[3].

The electron amplification is driven by the secondary electron emission (SEE). When an incident particle, such as electron and ion, collides with or goes through a solid surface, one or more secondary electrons are emitted[4]. The average number of secondaries produced per incident particle is the secondary-emission yield (SEY, δ). The energy distribution of the secondaries ($d\delta/dE$) is related to the energy of the incoming particle, the incident angle, the target material, etc.[5]. Bruining and Boer[6], Ushio et al.[7] and Jokela et al.[8] conducted target-shooting experiments using electron guns, and measured the SEY in the current mode. Olano and Montero[9] measured the energy distribution $d\delta/dE$ of Kapton, Teflon, and Ultem by charging analysis, and found the energy of secondaries to be much smaller than that of the primary electrons. Such results are then extrapolated to PMTs[10-11]. The low light intensity at which a PMT operates makes the incident electrons discrete. Therefore, one should be careful when extending the SEY from the current mode to a single electron case, the pulse mode.

While being amplified by the multiplier, a single PE induces numerous electrons, which are captured by the anode within a few hundred picoseconds. The initial energy of the PEs produced at the photocathode is $\sim 1\,\mathrm{eV}$[12]. The potential difference between the photocathode and the multiplier dominates the incident energy of the PEs arriving at the multiplier. Therefore, the amplifier provides nearly identical gain for the PEs. Because the total charge of the electrons captured by the anode is typically described by a Gaussian distribution in light of the central limit theorem of probability, the probability density function (PDF) of the single electron response (SER) charge distribution is $f_{\mathcal{N}}(Q; Q_1, \sigma_1^2)$,

where Q_1 is the mean charge, and σ_1 is its standard deviation. The PE count n_{PE} follows a Poisson distribution with the probability mass function $P_\pi(n_{\mathrm{PE}}; \lambda)$, where λ is the expected PE count at a certain light intensity. After amplification, the total charge distribution $f(Q)$ is a folding of the Poisson distribution and the SER charge distribution[3]. There are two types of background processes. The first one follows a low-charged finite-width Gaussian $\mathcal{N}(0, \sigma_0^2)$ without any PEs emitted from the photocathode. The second process is discrete with a probability w. Examples include thermoemission and noise generated by incident light. This discrete process follows an exponential distribution $\mathrm{Exp}(\alpha)$, with α being the rate of exponential decay. Considering the charge distribution of the two types of background processes being $f_{\mathrm{b}}(Q)$, the overall charge distribution can be expressed in Eq. (3.1):

$$
\begin{aligned}
f(Q) =& P_\pi(n_{\mathrm{PE}} = 0; \lambda)f_{\mathrm{b}}(Q) + \sum_{n_{\mathrm{PE}}=1}^{\infty} P_\pi(n_{\mathrm{PE}}; \lambda)f_{\mathcal{N}}(Q; n_{\mathrm{PE}}Q_1, n_{\mathrm{PE}}\sigma_1^2) \\
\approx& \left\{ \frac{(1-w)}{\sigma_0\sqrt{2\pi}} \exp\left(-\frac{Q^2}{2\sigma_0^2}\right) + w\theta(Q) \times \alpha \exp(-\alpha Q) \right\} e^{-\lambda} \\
&+ \sum_{n_{\mathrm{PE}}=1}^{\infty} \frac{\lambda^{n_{\mathrm{PE}}}e^{-\lambda}}{n_{\mathrm{PE}}!} \times \frac{1}{\sigma_1\sqrt{2\pi n_{\mathrm{PE}}}} \times \exp\left(-\frac{(Q-n_{\mathrm{PE}}Q_1)^2}{2n_{\mathrm{PE}}\sigma_1^2}\right)
\end{aligned}
\tag{3.1}
$$

where $\theta(Q)$ is the Heaviside function. When λ is less than 0.1, the probability of observing two or more PEs is less than one-tenth of the probability of observing a single PE. In this case, the charge distribution will only show the peak of the pedestal ($Q = 0$) and the peak of the single PE ($Q = Q_1$) as indicated in the blue histogram in Fig 3.1. We can obtain an approximate SER charge spectrum after applying some cuts to remove the pedestal. Our work aligns different PMTs' gain by dividing the SER charge spectrum with Q_1 as Q/Q_1. Instead of a large-sized dynode-chain commonly used in PMTs, MCP-PMTs employ MCPs as electron multipliers. MCP-PMTs are currently in use or planned for neutrino experiments like the Jiangmen Underground Neutrino Observatory (JUNO)[14] and the Jinping Neutrino Experiment[13], collider experiments like the Belle II TOP detector[15] and the PANDA DIRC Cherenkov detector at FAIR[16], and cosmic ray observatories like the Large High Altitude Air Shower Observatory[17]. Initially, the fact that the feedback ions cause damage to the photocathode led to a lifetime issue of MCP-PMTs[18].

The atomic layer deposition (ALD) technique[10] is applied to fabricate MCP-PMTs solving the lifetime issue[19]. Chen et al.[2] indicated that depositing high SEY materials such as Al_2O_3 via ALD on the input electrode of the first MCP can enhance the probability
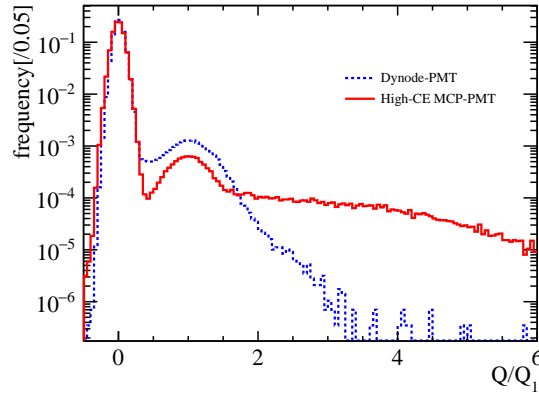
Figure 3.1 The charge spectrum of the high-CE MCP-PMT GDB-6082 (red) and a dynode-PMT (blue)[13]. The blue histogram consists of the pedestal $Q = 0$ and the principal peak of $Q = Q_1$, while the red histogram includes jumbo charges.

of collecting the secondaries to improve CE to nearly 100 % rather than being constrained by the MCP open-area ratio. This enhancement is later extended to a composite Al_2O_3-MgO layer by Cao et al.[20] and Zhang et al.[21] to allow for increased gain, improved single electron resolution, and a higher peak-to-valley ratio of the MCP-PMTs[11].

In the performance tests to evaluate the 8-inch high-CE MCP-PMT by the Jinping Neutrino Experiment, *jumbo charges* are found in the SER charge spectra[13], as shown in the red histogram in Fig 3.1. Similar charges have also been observed in the mass testing of the 20-inch MCP-PMTs at JUNO, identified as the "long tail" in the SER charge distribution[22]. Orlov et al.[23] reported that the pulse height distribution of the high-CE MCP-PMTs had a non-Gaussian long-tail structure. Zhang et al.[24] used the charge model in Eq. (3.1) for the jumbo charges and recommended an extra gain calibration. Yang et al.[25] conducted a voltage-division experiment to reveal that the MCP gain for the low-energy electrons is significantly smaller than that for the high-energy ones. Thus, the MCP gain for the secondaries differs from that for the PEs entering the channels directly. The SER charge model in Eq. (3.1) is no longer sufficient to accurately calibrate this type of PMT. Understanding the origin of the jumbo charges is necessary for an appropriate SER charge calibration.

To elucidate the nature of the jumbo charges, the Gamma distribution is introduced and a voltage-division experiment is developed to measure the relationship between MCP gain and the energy of the incident electrons. Considering the SEE model, we elucidate the nature of the jumbo charges and calculate the total SEY of the Al_2O_3-MgO layer when the incident energy is $650 \, eV$. Through convolution-based modeling, the physical mechanisms driving have been clarified, and a quantitative mathematical framework establishe,

5

which is the first formulation for these kind of high-CE MCP-PMTs.

3.1.1 Gamma-Distributed SER charges

Every multiplication of electrons at the dynodes or MCP channels follows approximately a Poisson distribution[26]. A series of such multiplications forms cascaded Poissonians[1] and is an example of the branching process[27] challenging to perform analytical computations. Woodward[28] argued that the SER charge spectrum exhibits an intermediate shape between a Poisson and a Gaussian. Prescott[29] proposed a cascaded Polya distribution to characterize the electron multiplication in PMT, particularly when considering the non-uniformity of the dynode surface. Kalousis[30-31] approximated the Polya distribution as a Gamma one to calibrate PMT and achieved better results than the Gaussian model in Eq. (3.1).

Instead of the Gaussian containing a small nonphysical tail less than 0, we choose a Gamma distribution $\Gamma(\alpha, \beta)$ defined by the scale factor α and the rate factor β, as shown in Eq. (3.2):

$$f_\Gamma(x; \alpha, \beta) = \frac{x^{\alpha-1} e^{-\beta x} \beta^\alpha}{\Gamma(\alpha)} \quad \text{for } x > 0 \quad \alpha, \beta > 0 \tag{3.2}$$

where $\Gamma(\alpha)$ is the Gamma function. A Gamma distribution is uniquely determined by its expectation value $\alpha/\beta = Q_1$ and variance $\alpha/\beta^2 = \sigma_1^2$, which can be converted into the Gaussian counterparts in Eq. (3.1). The charge spectrum based on the Gamma distribution is,

$$f(Q) = P_\pi(n_{\text{PE}} = 0; \lambda) f_b(Q) + \sum_{n_{\text{PE}}=1}^{\infty} P_\pi(n_{\text{PE}}; \lambda) f_\Gamma(Q; n_{\text{PE}}\alpha, \beta). \tag{3.3}$$

3.1.2 Jumbo Charges through Extra Multiplication

SEE has received considerable attention during the widespread application of electronic tubes. Bruining summarized the SEE's methods, findings, and applications in his classic *Physics and Applications of Secondary Electron Emission*[32]. Baroody[33] put forward his SEE theory of metals assuming that an incident primary electron interacts only with free electrons in the conduction band, without considering the variation of secondary emission with the primary energies. Dekker et al.[34] presented the SEE quantum theory of the Coulomb interaction between the incident primaries and the lattice electrons. Wolff[35] provided the cascade theory for the diffusion, the energy loss, and the multiplication of the secondary electrons within a metal. Assuming both incident and back-

scattered electrons within the target are isotropic, Kanaya et al.[36] calculated the SEY from insulators with the ionization potential by setting the valence electron and the back-scattered coefficient besides the parameter of the free-electron density effect. Vaughan[37] formulated the SEY as a function of impact energy and direction used in computer programs, known as the *Vaughan model*. Furman and Pivi[5] developed a mathematically self-consistent Monte Carlo program to elucidate the SEE phenomenon from solid surfaces usually called the *Furman model*. This model incorporates the statistical nature of the SEE process by considering the probability distribution governing the number of the secondaries emitted per incident primary electron. The energies of secondary electrons are approximated as independent and identically distributed random variables determined by the material properties and the primary energies.

Early models primarily focused on theoretical explanations of SEE. The Vaughan and Furman models emphasize the Monte Carlo computation instead. Comparatively, the Furman model strives for physical consistency and better agreement with experiments. Therefore, we choose it for more adjustable parameters and higher accuracy.

3.1.2.1 Furman probabilistic model

In the Furman model[5], there are three kinds of secondary electrons. The first is the back-scattered electron, emitted through elastic scattering on the surface of the target material. The energy distribution $\mathrm{d}\delta_{\mathrm{bs}}/\mathrm{d}E$ is defined in Eq. (3.4), where δ_{bs} is the yield of the back-scattered electron, the Heaviside function $\theta(E)$ ensures the $E < E_0$. E_0 is the incident energy of the primary electron, θ_0 is the incident angle, and σ_{bs} is an adjustable standard deviation.

$$\frac{\mathrm{d}\delta_{\mathrm{bs}}}{\mathrm{d}E} = \theta(E)\theta\left(E_0 - E\right)\delta_{\mathrm{bs}}\left(E_0, \theta_0\right)\frac{2\exp\left(-\left(E - E_0\right)^2/2\sigma_{\mathrm{bs}}^2\right)}{\sqrt{2\pi}\sigma_{\mathrm{bs}}\,\mathrm{erf}\left(E_0/\sqrt{2}\sigma_{\mathrm{bs}}\right)} \tag{3.4}$$

After penetrating the target material, some electrons are inelastically scattered by the atoms and are reflected out to form the second category. Lenard called the bending of the electron track "diffusion", and the trajectory turning 90° as "Rückdiffusion" in German literature[32]. Furman and Pivi[5] adopted this convention to name them as the *rediffused electrons*. The energy distribution of the rediffused electrons is defined as Eq. (3.5), where δ_{rd} is the yield of rediffused electron, and q is an adjustable parameter.

$$\frac{\mathrm{d}\delta_{\mathrm{rd}}}{\mathrm{d}E} = \theta(E)\theta\left(E_0 - E\right)\delta_{\mathrm{rd}}\left(E_0, \theta_0\right)\frac{(q + 1)E^q}{E_0^{q+1}} \tag{3.5}$$

The final and most important kind is the true-secondary electrons. Upon deeper penetration of electrons into the target material, intricate physical processes ensue, generating one or more secondaries. This is the process of multiplying electrons. The spectrum is defined as Eq. (3.6).

$$\frac{\mathrm{d}\delta_{\mathrm{ts}}}{\mathrm{d}E} = \sum_{n=1}^{\infty} \frac{n P_{n,\mathrm{ts}}\left(n; \delta_{\mathrm{ts}}(E_0, \theta_0)\right)\left(E/\epsilon_n\right)^{p_n-1} e^{-E/\epsilon_n}}{\epsilon_n \Gamma\left(p_n\right) \Upsilon\left(np_n, E_0/\epsilon_n\right)} \times \Upsilon\left[(n-1)p_n, \left(E_0 - E\right)/\epsilon_n\right] \quad (3.6)$$

where $\delta_{\mathrm{ts}}(E_0, \theta_0)$ is the yield of the true-secondary electrons when the incident energy is E_0 and the incident angle is θ_0, $\epsilon_n > 0$ and $p_n > 0$ are the phenomenological parameters. $\gamma(z, x)$ is the incomplete gamma function, and $\Upsilon(z, x) = \gamma(z, x)/\Gamma(z)$ is the normalized form satisfying $\Upsilon(0, x) = 1$. n, the number of the true-secondary electrons, follows a Poisson distribution $(\delta_{\mathrm{ts}}(E_0, \theta_0))$. $P_{n,\mathrm{ts}}$ is its probability mass function.

As illustrated in Fig. 3.2, we set the parameters as $\delta_{\mathrm{bs}} = 0.05$, $\delta_{\mathrm{rd}} = 0.5$, $\delta_{\mathrm{ts}} = 5$[11], $\theta_0 = 0°$ and $E_0 = 650\,\mathrm{eV}$. The total spectrum is $\mathrm{d}\delta/\mathrm{d}E = \mathrm{d}\delta_{\mathrm{bs}}/\mathrm{d}E + \mathrm{d}\delta_{\mathrm{rd}}/\mathrm{d}E + \mathrm{d}\delta_{\mathrm{ts}}/\mathrm{d}E$. The energies of the secondaries are usually less than $100\,\mathrm{eV}$ when the incident energy E_0 is $650\,\mathrm{eV}$.
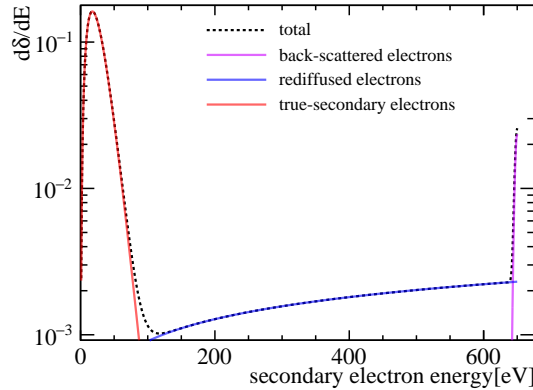

Figure 3.2 The total energy spectrum of the secondary electrons when the incident energy is 650 eV. The violet, blue, and red lines represent $\mathrm{d}\delta_{\mathrm{bs}}/\mathrm{d}E$, $\mathrm{d}\delta_{\mathrm{rd}}/\mathrm{d}E$, and $\mathrm{d}\delta_{\mathrm{ts}}/\mathrm{d}E$, repectively. The black dashed line is $\mathrm{d}\delta/\mathrm{d}E$.

3.1.2.2 An extra multiplication mode

The MCP-PMT under study uses a Chevron stack of two MCPs as the electron multiplier. As shown in Fig. 3.3, an Al_2O_3-MgO-Al_2O_3 layer[21] is deposited on the channel surface of the lead glass body and on the entrance electrode M1 of the first MCP through the ALD technology. There are two alternative routes of amplification for every PE: the *channel mode*, where the PE directly enters a channel, and the *surface mode*, where the

secondaries from M1 enter the MCP channels under the focusing electric field. The selection of these two routes is a Bernoulli trial[1].

The MCP gain for those low-energy secondaries in the surface mode is substantially smaller than that for the primary PEs in the channel mode[10].

3.1.2.3 Voltage-division Experiment

The dependence of the MCP gain for an electron versus its incident energy at the channel entrance is crucial to understanding the jumbo charges. We designed a voltage-division experiment to measure such a relationship.

As shown in Fig 3.3, we utilized a positive high-voltage power supply (positive HV) to stabilize the potentials applied to the MCPs through the circuit[38]. In parallel, we took a negative high-voltage power supply (negative HV) to vary the electric potential difference between the photocathode and M1 to get PEs at different incident energies. Compared to the experiment of Yang et al.[25] where the potentials of all the electrodes M1-4 are controllable, our design is a simplified adaptation only to tune the energies of the PEs with commercially available HV products.

We used a picosecond laser with a wavelength of 405 nm to illuminate the MCP-PMT at 1 kHz rate and feed an electronic trigger signal to capture waveform data. To obtain the single PE, we adjusted the intensity of the laser until the occupancy was below 0.1. We deployed a 10-bit oscilloscope (HDO9000 with HD1024 Technology)[39] to capture the 100 ns waveform with a sampling rate of 40 GS/s and a range of [-20, 60] mV.

We obtained the gain of the MCP-PMTs at different energies of the incident electrons by fitting the Gaussian on the charge distribution, and conducted the same experiment on two MCP-PMTs with (Fig. 3.4(b)) and without (Fig. 3.4(a)) Al_2O_3-MgO deposited on M1 to contrast the effect of the surface mode. The positive voltages for the MCP-PMT with and without Al_2O_3-MgO on M1 are +1205 V and +1240 V, respectively. The initial energies of the PEs are ~1 eV[12] and the systematic error of the negative HV itself is within 2 V. The incident energies (E_0) are defined as the energies acquired by the PEs in the electric field, numerically equal to the potential difference between the photocathode and M1, with an error of ± 2 eV. We scanned the MCP gain and measured it every 10 eV when $10 \leqslant E_0 < 100$ eV, every 20 eV when $100 \leqslant E_0 < 200$ eV and every 50 eV when $200 < E_0 \leqslant 650$ eV. For the MCP-PMT with Al_2O_3-MgO deposited on M1, our scan range is $10 \leqslant E_0 \leqslant 600$ eV. For the MCP-PMT without, the range is $10 \leqslant E_0 \leqslant 680$ eV.

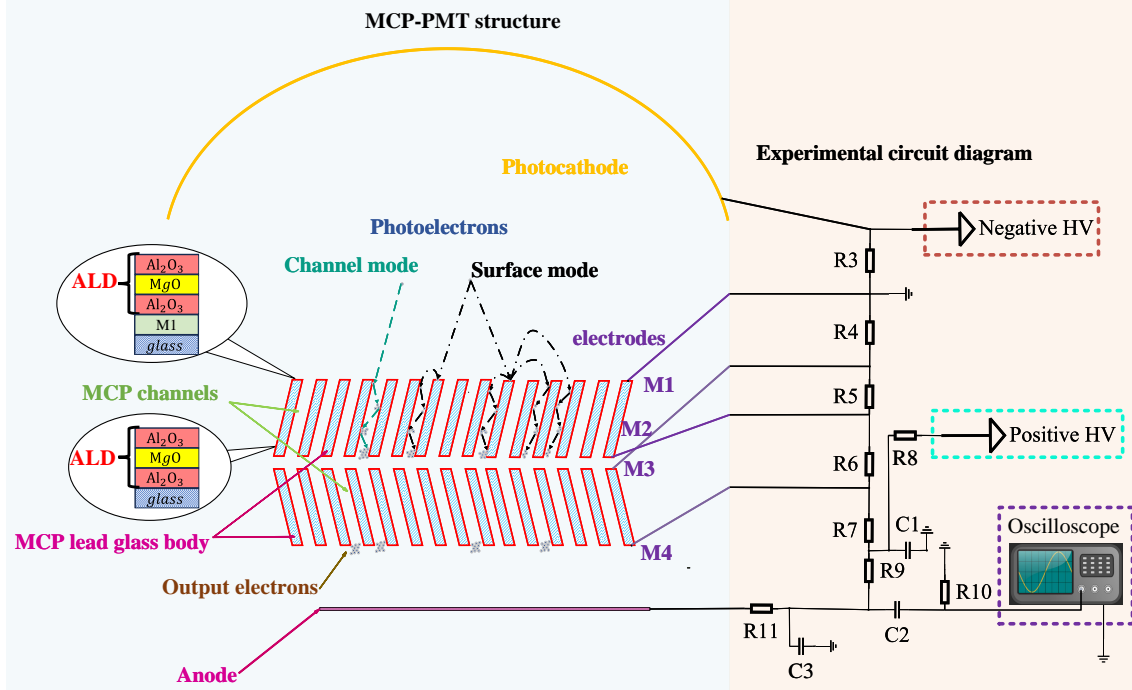The charges of the captured waveforms were measured with *fast stochastic matching*

Figure 3.3   M1 and M3 are the input electrodes of MCPs, M2 and M4 are the output electrodes, and the four electrodes provide the potential differences during operation. The PEs directly enter the channels (channel mode) or hit M1 to produce secondary electrons that enter the channels later (surface mode)[2]. After entering the MCP channel, the electron collides with the channel wall many times and is amplified in a series of such multiplications[1]. Our circuit design was modified from the circuit implementation in the reference[38]. We removed useless R1 and R2 in our circuit design, while the rest of the resistors remained unchanged.

pursuit (FSMP)[40-41], which suppresses the interference of electronic noise to give accurate charge spectra under a wide range of gain. Due to FSMP's ability to count PEs, the charge would be 0 when $n_{PE} = 0$ and the pedestal is cleanly cut out in the output charge distribution. In Fig. 3.4, the peaks are attributed to the channel mode. The jumbo charges from the surface mode are to the right and deficient amplifications are to the left of the peaks. Due to the small contribution of secondaries from the surface mode for the MCP-PMT without Al_2O_3-MgO deposited on M1, there is no jumbo charge in the charge spectrum, as shown in Fig. 3.4(a). To obtain the MCP gain for the electrons directly entering the channels, we only fitted the peak to exclude the influence of the surface mode.

We obtained approximate values of μ_p and σ_p of the charge distribution to provide initial values and ranges for a detailed fit. The fit ranges were determined from the incident energies of the PEs, when $E_0 > 100$ eV, it was $[\mu_p - 1.3\sigma_p, \mu_p + 1.6\sigma_p]$; when $30 < E_0 \leqslant 100$ eV, $[\mu_p - 0.8\sigma_p, \mu_p + 1.6\sigma_p]$; and when $E_0 \leqslant 30$ eV, $[\mu_p - 1.5\sigma_p, \mu_p + 1.8\sigma_p]$. It is sufficient to extract the mean charge $\mu(E_0)$ and the standard deviation $\sigma(E_0)$ of the channel-mode peak to measure the MCP gain for electrons at different energies.
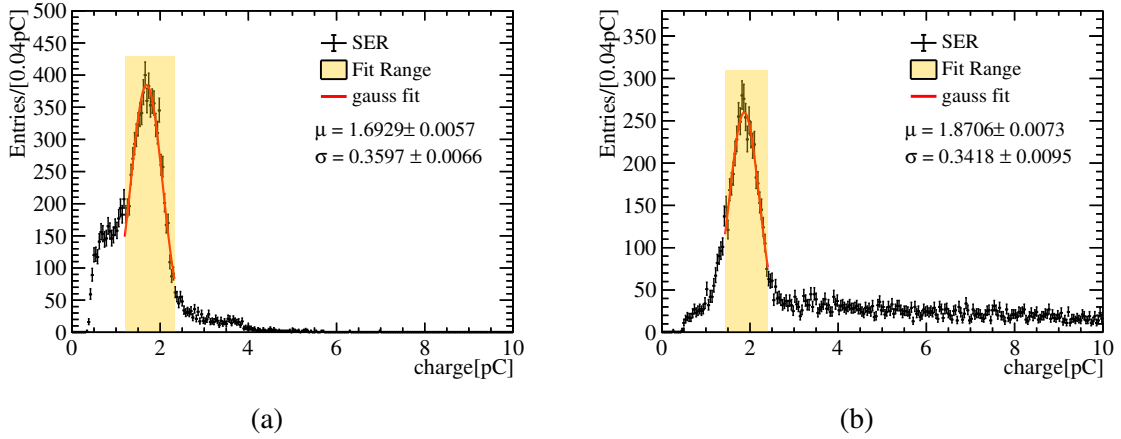
Figure 3.4   Fit of the charge spectrum of the MCP-PMT without (a) and with (b) Al_2O_3-MgO deposited on M1. We observed that (a) does not exhibit jumbo charges. The yellow areas are incident energy-dependent intervals and the red lines are fitting results of the Gaussian functions in the intervals.

After fitting with Gaussians, we interpolate and extrapolate linearly to obtain the relations of $\mu(E_0)$ and $\sigma(E_0)$ in Fig. 3.5. The difference in the relations of MCP-PMTs with and without Al_2O_3-MgO deposited on M1 comes from the influence of the charge contributed from the surface mode. When $E_0 < 200\,\text{eV}$, $\mu(E_0)$ rapidly increases. As $E_0 > 200\,\text{eV}$, $\mu(E_0)$ gradually stabilizes. The $\sigma(E_0)$ is overall increasing similar to $\mu(E_0)$ but sees a drop around 200 eV. A similar trend of $\mu(E_0)$ is reported by Yang et al.[25]. In our case, the best relative resolution σ/μ is at around 600 eV and Yang et al.'s results suggested 200 eV. Cao et al.[20] found that the SEY of Al_2O_3-MgO increases with the incident energy in 100–600 eV. Even though the film structure and thickness we used are different, we can still make a rough assessment that the trend of σ/μ obtained here is reasonable, considering the variation curves of the SEY of Al_2O_3 and MgO with energy.

3.1.2.4 Charge-Spectra Decomposition

The Furman model in Sec. 3.1.2.1 predicts the energies of the secondaries. Our voltage-division experiment in Sec. 3.1.2.3 measured the relationship between the MCP gain and the incident energies of the electrons. We follow the flowchart in Fig. 3.6 to calculate the charge distribution by Monte Carlo. In this study, we shone the laser at the apex of the photocathode hemisphere, and the PEs hit M1 with an incident angle $\theta_0 = 0°$. The complex amplification process in the channels is described by the incident energy-dependent Gamma distributions $\Gamma(\alpha(E), \beta(E))$ described in Sec. 3.1.1. The $\alpha(E)$ and $\beta(E)$ are estimated with the relations of $\mu(E)$ and $\sigma(E)$ of MCP-PMT without Al_2O_3-MgO coating on the input electrode, which eliminates the influence of the surface mode.
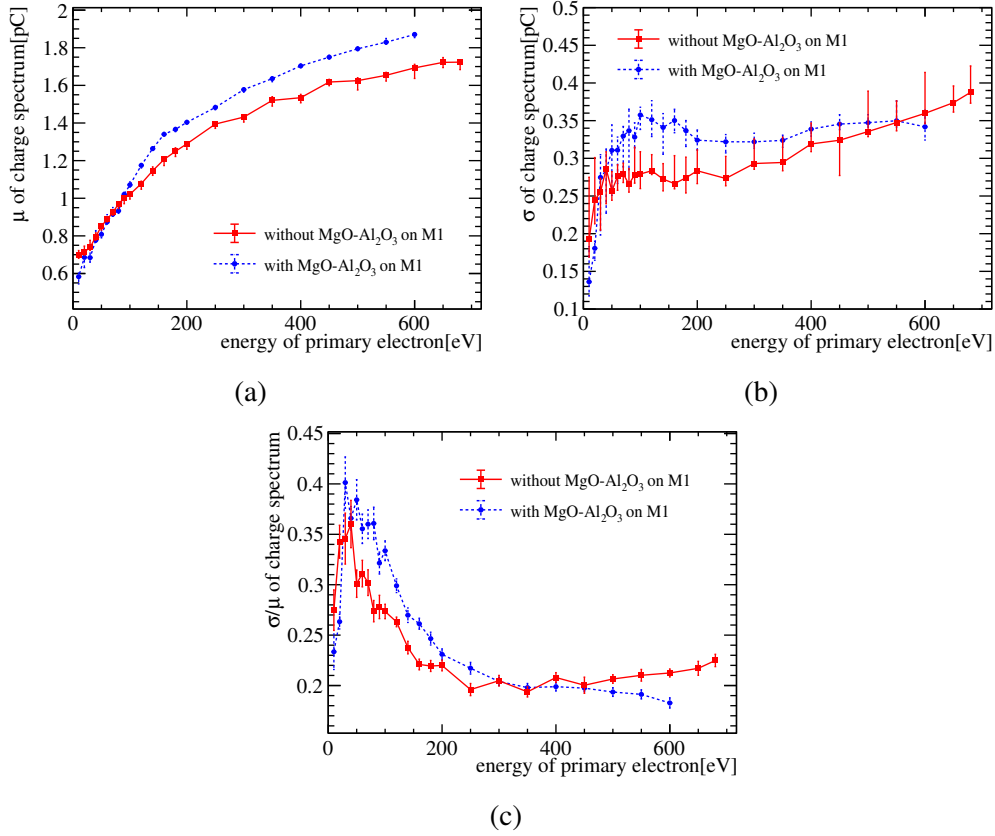
(a)

(b)

(c)

Figure 3.5   (a) The mean μ increases as the incoming electron energy E_0 increases. (b) The standard deviation σ changes with energy. The MCP-PMT with Al_2O_3-MgO deposited on M1 (the red line) shows a similar variation trend to the one without (the blue line). (c) The resolution σ/μ increases between 0-50 eV, decreases between 50-400 eV, and after 400 eV, there is a slight decrease for those with Al_2O_3-MgO deposited on M1 (the blue line) and a slight increase for those without (the red line).

Taking into account the light intensity, we repeatedly sample n_{PE} from the Poisson distribution and sum up n_{PE} SER charges for the output to get a spectrum.

For sampling an SER charge, we assign the probabilities of the channel and surface modes as p and $1 - p$ for a Bernoulli trial. The SER charge spectrum $f_{MCP-PMT}(Q)$ is

$$f_{MCP-PMT}(Q) = pf_{ch}(Q) + (1 - p)f_{surf}(Q) \qquad (3.7)$$

where $f_{ch}(Q)$ and $f_{surf}(Q)$ are the charge distributions of the channel and surface modes. $f_{ch}(Q)$ is set to $f_\Gamma(Q; \alpha(E_0), \beta(E_0))$, with the incident energy being 650 eV. The factors $\alpha(E_0), \beta(E_0)$ are converted from $\mu(E_0)$ and $\sigma(E_0)$ without Al_2O_3-MgO coating in Fig. 3.5.

The $f_{surf}(Q)$ is divided into three components by the Furman model corresponding to Eqs. (3.4)–(3.6), $f_{bs}(Q)$ for the back-scattered electrons, $f_{rd}(Q)$ for the rediffused elec-
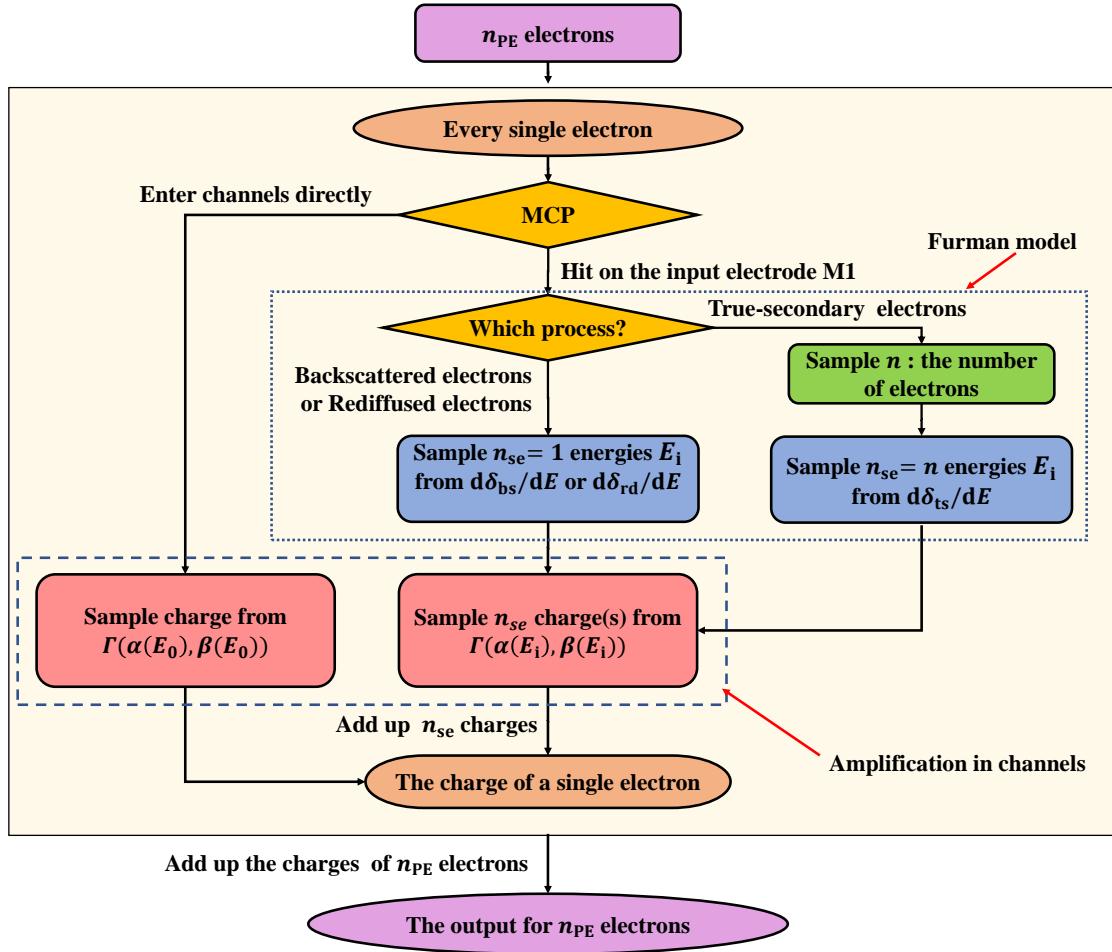
Figure 3.6 The flowchart of Monte Carlo to compute the charge spectrum. The output charge consists of n_{PE} SER charges. The PEs in the channel mode enter channels directly, while PEs in the surface mode hit the input electrode. The energies of the n_{se} secondaries in the surface mode are sampled from the Furman model. The amplification in channels is modeled by the incident energy-dependent Gamma distribution.

trons, and $f_{ts}(Q)$ for the true-secondary electrons.

$$
\begin{aligned}
f_{surf}(Q) &= p_{bs}f_{bs}(Q) + p_{rd}f_{rd}(Q) + (1 - p_{bs} - p_{rd})f_{ts}(Q) \\
&= \delta_{bs}f_{bs}(Q) + \delta_{rd}f_{rd}(Q) + (1 - \delta_{bs} - \delta_{rd})f_{ts}(Q)
\end{aligned}
\tag{3.8}
$$

where p_{bs} and p_{rd} are the mixture ratios determined by the composition and thickness of surface emissive material that varies among the PMTs. Furman and Pivi[5] assume that only one electron is emitted in back-scattered mode and rediffused mode so that $\delta_{bs} = p_{bs}$ and $\delta_{rd} = p_{rd}$. In the calculation, we specify $\delta_{rd} = 0.09$ and $\delta_{bs} = 0.01$. The energy of the back-scattered electron is nearly equal to that of the PEs in the channel mode, and so is the MCP gain for them. The energy of the rediffused electron is lower – from $100\,\text{eV}$ to $600\,\text{eV}$, causing the charge after MCP multiplication to be slightly smaller thanks to the relatively slow increase of gain in that range in Fig. 3.5(a). Either contributes a single

electron and is practically indistinguishable from the channel mode in the charge spectra. Such a degeneracy is summarized in Eq. (3.9):

$$
\begin{aligned}
f_{\text{MCP-PMT}}(Q) &= p f_{\text{ch}}(Q) + (1-p) f_{\text{surf}}(Q) \\
&= p f_{\text{ch}}(Q) + (1-p)[\delta_{\text{bs}} f_{\text{bs}}(Q) + \delta_{\text{rd}} f_{\text{rd}}(Q) + (1 - \delta_{\text{bs}} - \delta_{\text{rd}}) f_{\text{ts}}(Q)] \\
&= [p + (1-p)(\delta_{\text{bs}} + \delta_{\text{rd}})] f_{\text{ch}}(Q) + (1-p)(1 - \delta_{\text{bs}} - \delta_{\text{rd}}) f_{\text{ts}}(Q)
\end{aligned}
$$
(3.9)

where the spectra $f_{\text{ch}}(Q)$, $f_{\text{rd}}(Q)$ and $f_{\text{bs}}(Q)$ are merged into $f_{\text{ch}}(Q)$.

Nevertheless, Eq. (3.9) is incomplete. We should consider the case when the secondaries hit the MCP surface again. The round trip does not inject extra energy. A backscattered or rediffused secondary gets amplified essentially in the same way as a primary PE, while a true-secondary electron has too low energy to multiply again. Therefore, p_0, the net contribution to $f_{\text{ch}}(Q)$, is a geometric series

$$
p_0 = p \sum_{i=0}^{\infty} [(1-p)(\delta_{\text{bs}} + \delta_{\text{rd}})]^i = \frac{p}{1 - (1-p)(\delta_{\text{bs}} + \delta_{\text{rd}})}
$$
(3.10)

and $f_{\text{ts}}(Q)$ gets $\frac{(1-p)(1-\delta_{\text{bs}}-\delta_{\text{rd}})}{1-(1-p)(\delta_{\text{bs}}+\delta_{\text{rd}})}$ or $1 - p_0$. Eq. (3.9) is remarkably reduced to

$$
f_{\text{MCP-PMT}}(Q) = p_0 f_{\text{ch}}(Q) + (1 - p_0) f_{\text{ts}}(Q).
$$
(3.11)

In the case of the true-secondary electrons, their count n follows a Poissonian. The sum of the sampled n charges serves as the output Q_{ts},

$$
\begin{aligned}
Q_{\text{ts}} &= \sum_{i=1}^{n} Q_i \\
n &\sim \ (\delta_{\text{ts}}') \\
Q_i &\sim \Gamma[\alpha(E_i), \beta(E_i)]
\end{aligned}
$$
(3.12)

where E_i are sampled from Eq. (3.6). $\alpha(E_i)$ and $\beta(E_i)$ are converted from $\mu(E_i)$ and $\sigma(E_i)$ of Fig. 3.5. For completeness, $\delta_{\text{ts}} = (1 - \delta_{\text{bs}} - \delta_{\text{rd}})\delta_{\text{ts}}'$ is the electric-current ratio of the true-secondary electrons to that of the primary.

The charge spectra of different n are shown in Fig. 3.7(a). Due to the lower energies of the secondaries, their charges are smaller. It is challenging to distinguish each charge formed at the anode, as multiple secondary electrons enter the MCP channels simultaneously. Bigger n results in a larger charge.

A typical decomposition of the SER charge spectra is shown in Fig. 3.7(b). The jumbo charges, also known as the "long tail", are contributed by the true secondaries from the surface mode.
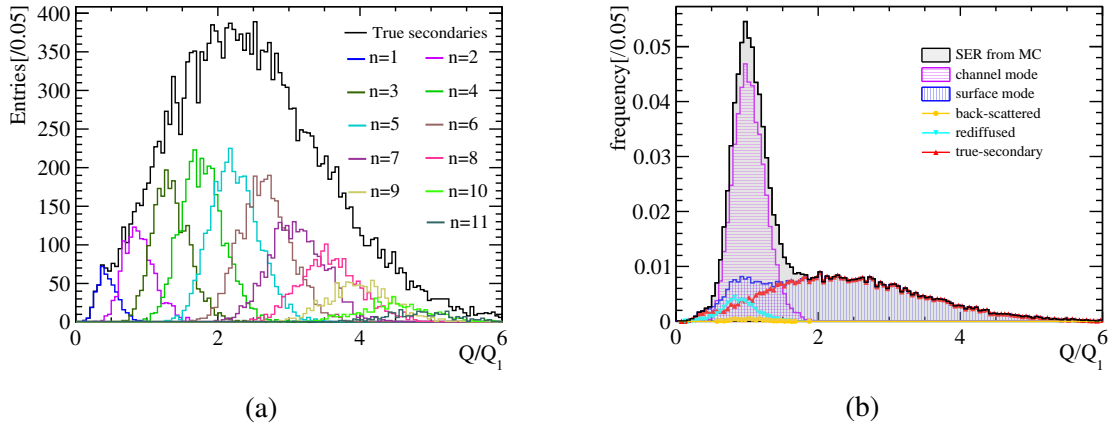
(a)

(b)

Figure 3.7 (a): The charge distribution of the true-secondary electrons mode in the MC calculation when $\delta'_{ts} = 5.5$ and $p_0 = 0.55$. The black histogram gives the sum of all the distributions. (b): The charge distribution formed in the channel mode is concentrated around the peak, while the tail portion is mainly generated by the true-secondary electrons in the surface mode.

3.1.3 Parameter Extraction from Data

It is evident from Eq. (3.11) and (3.12) that δ'_{ts} and p_0 significantly impact the SER charge distribution, demonstrated in Fig. 3.8. We use the MCP-PMT test data by Zhang et al.[13] to determine the two parameters.

(a)

(b)
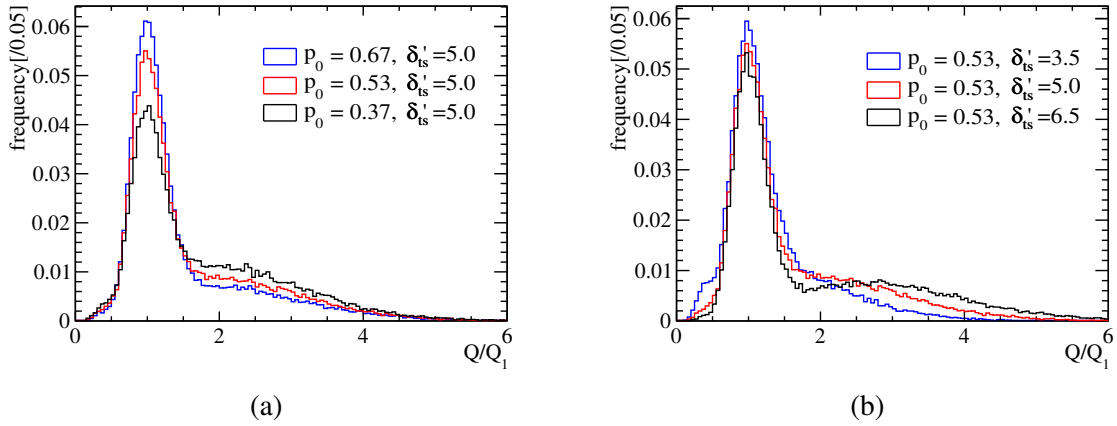
Figure 3.8 δ'_{ts} and p_0 influence the shape of SER charge spectrum from MC. As δ'_{ts} increases, the region of the tail becomes more prolonged. As p_0 increases, the height of the principal peak region increases, and the tail becomes narrower.

Between each pair of predicted and measured charge distributions, we perform a chi-square test. These two histograms are divided into r bins using the same binning method. The entries in the i-th bin are n_i and m_i, adding up to $N = \sum_{i=1}^{r} n_i$ and $M = \sum_{i=1}^{r} m_i$. The chi-square test indicates the similarity between two histograms[42],

$$\chi^2_{r-1} = \sum_{i=1}^{r} \frac{\left(n_i - N\hat{k}_i\right)^2}{N\hat{k}_i} + \sum_{i=1}^{r} \frac{\left(m_i - M\hat{k}_i\right)^2}{M\hat{k}_i} = \frac{1}{MN} \sum_{i=1}^{r} \frac{\left(Mn_i - Nm_i\right)^2}{n_i + m_i} \qquad (3.13)$$

15

where $\hat{k}_i = \frac{n_i + m_i}{N + M}$.

The χ^2_{r-1} are scanned in the (p_0, δ'_{ts}) grid, with an example in Fig. 3.9(a). We use a linear model[43] to smooth the approximate parabolic relationship between the χ^2_{r-1} and (p_0, δ'_{ts}), then extract the $(\hat{p}_0, \hat{\delta}'_{ts})$ that minimizes χ^2_{r-1} with intervals at 68.3 % confidence levels[44].
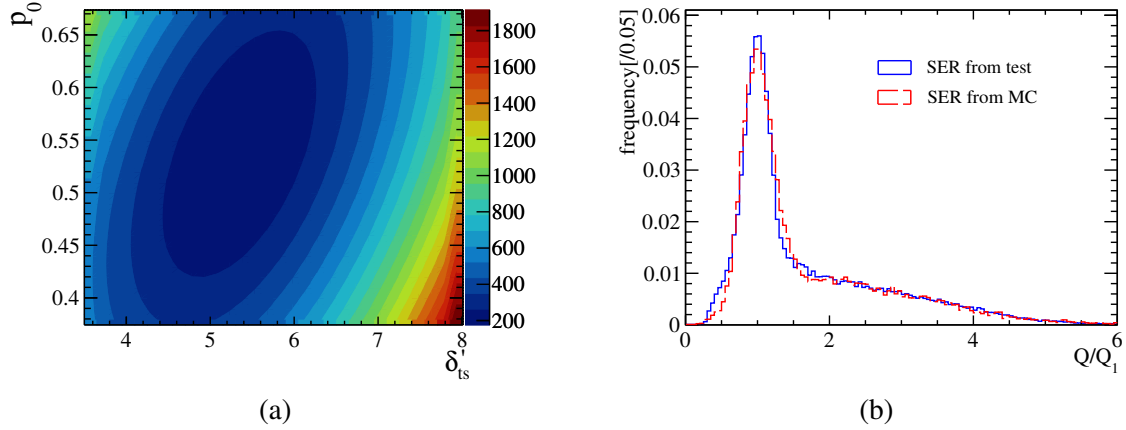

(a)	(b)

Figure 3.9   The plot (a) is the contour plot of the chi-square test, with p_0 and δ'_{ts} as parameters and the chi-square values as the height. The plot (b) is an example of the MC histogram (the red line) and the histogram from test (the blue line).

The $\hat{\delta}'_{ts}$ vs. $\hat{p}_0$ scatter plot of 9 MCP-PMTs in Fig. 3.10 does not indicate a strong correlation. They are determined by independent manufacturing stages. On average, δ'_{ts} is 5.979 and p_0 is 0.5341. The PEs of the channel, back-scattered, and rediffused surface modes account for 53.41 %. They constitute the peak. Each of the rest hits the surface to induce 5.979 true-secondary electrons on average.
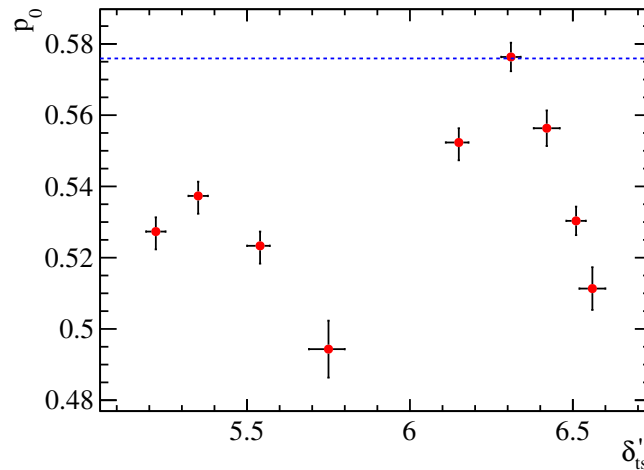

Figure 3.10   When convolving with 9 MCP-PMTs, the distribution of δ'_{ts} and p_0 at the minimum chi-square occurs. The blue dashed line shows the expected $\hat{p}_0$ estimated from[45].

To compare our measurement to previous studies, we convert δ'_{ts} to the SEY δ

$$\delta = \delta_{bs} + \delta_{rd} + (1 - \delta_{bs} - \delta_{rd})\delta'_{ts} \tag{3.14}$$

and the fraction p_0 to p by Eq. (3.10). Cao et al.[20] measured the SEY of Al_2O_3-MgO double-layered film to be 4–5. Chen et al.[2] pointed out that there is an electrostatic lens effect at the MCP channel entrances, making the ratio of the PEs entering the MCP channels smaller than the open-area ratio. When PEs come with an incident angle $\theta_0 = 0°$, the proportion of the PEs directly entering the MCP channels is around 60 % when the MCP open-area ratio is 74.9 %. Chen et al.[45] indicated that the proportion is around 55 % when the open-area ratio is 65 %. The MCPs in our case have pore diameters of 12 m, spacings of 14 m between the pores, and open-area ratios of 66.6 %. The expected $\hat{p}_0 = \frac{55\%}{1-(1-55\%)(\delta_{rd}+\delta_{bs})} \approx 57.6\%$ for $\delta_{rd} + \delta_{bs} = 0.1$.
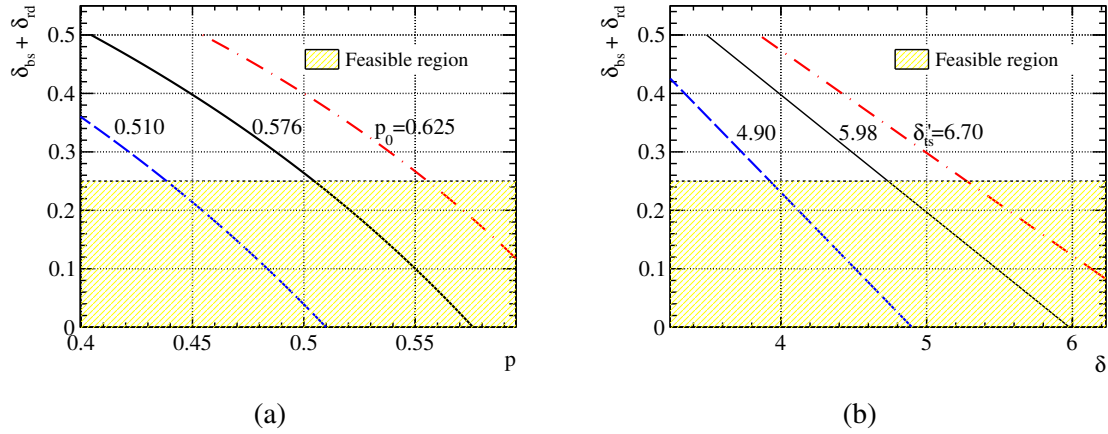

Figure 3.11   Relations of $\delta_{bs} + \delta_{rd}$ against the SEY δ and the fraction of channel mode p. The feasible region shows the consistency of our measurement to the literature.

In Fig. 3.11, with the typical values of $\delta = 5$ and $p = 0.55$, our measurement is consistent with an assumption that $\delta_{bs} + \delta_{rd} < 0.25$. The small contribution of the back-scattered and rediffused electrons in SEE is pointed out by Beck[46] to be especially true for insulators with high SEY.

3.1.4 Gamma-Tweedie model for MCP-PMT

In our calculation, the distribution of the MCP charge response to the true-secondary electrons $\Gamma(\alpha_i, \beta_i)$ is determined by their energies E_i, which satisfy $\sum_i^n E_i < E_0$. The incident energy E_0 of the PEs is 650 eV, which is more than ten times the energies of the true secondaries. Because n follows a Poisson distribution with an expectation between 5 and 6.5, the probability of n exceeding 10 is negligible. Thus, the effect of n

on E_i can be ignored, and the energy E_i is independently and identically distributed, as demonstrated in Fig. 3.12(a). The charge response of MCP to a single true-secondary electron, in turn, can be treated identically, as shown in Fig. 3.12(b). Furthermore, a single Gamma distribution $\Gamma(\alpha', \beta')$ is flexible enough to describe the continuous mixture of $\int dE_i \frac{1}{\delta_{ts}} \frac{d\delta_{ts}}{dE_i} \Gamma[\alpha(E_i), \beta(E_i)]$.
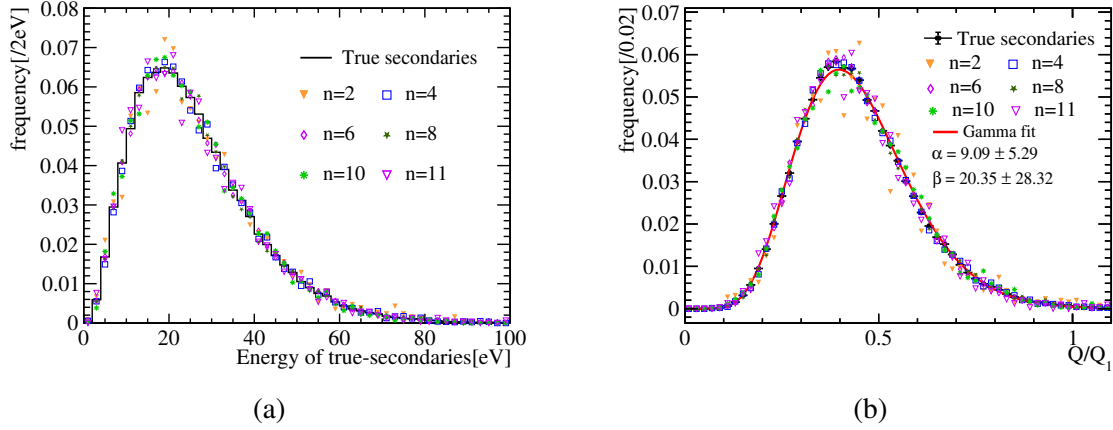

Figure 3.12   The energy distribution and the charge response distribution of MCP to a single true-secondary electron when n is different. (a): All the energies of the true secondaries follow the same distribution, although n is different. (b): the charge response of MCP to a single true-secondary electron is identical, and the fitting of the Gamma distribution $\Gamma(\alpha', \beta')$ achieves sufficient goodness.

When we use such a single $\Gamma(\alpha', \beta')$ in Eq.(3.12), the resulting Poisson-Gamma compound is a special case of the Tweedie distribution $\text{Tw}_\xi(\alpha, \beta)$ for $1 < \xi < 2$[47].

$$\left. \begin{array}{r} Q_{ts} = \sum_{i=1}^{n} Q_i \\ n \sim (\delta'_{ts}) \\ Q_i \sim \Gamma(\alpha', \beta') \end{array} \right\} \implies Q_{ts} \sim \text{Tw}_\xi(\alpha', \beta') \tag{3.15}$$

A phenomenological joint fit of the f_{ch} Gamma and f_{ts} Tweedie mixture with Eq. (3.11) and (3.15) is sufficient to calibrate the SER charge spectrum and measure p_0 and δ'_{ts}. The voltage division experiment (Sec. 3.1.2.3) relations $\mu(E_i)/\sigma(E_i)$ and the Furman model provide the understanding of the jumbo charges and the justification of the phenomenological Gamma-Tweedie mixture, but are less practically useful in PMT calibrations.

The number of parameters, 2 for f_{ch} Gamma and 3 for f_{ts} Tweedie, hinders convergence unless we aid it with physical constraints. Typically $\frac{\alpha'}{\beta'} \approx 0.45 Q_1$ and $\sqrt{\frac{\alpha'}{\beta'^2}} \approx 0.15 Q_1$. It is practical to bound them in $[0.3, 0.7]Q_1$ and $[0.05, 0.3] Q_1$ when the incident energy E_0 is significantly greater than E_i. We also have checked the chi-square results in the Gamma-Tweedie fitting, which gives good $\chi^2/\text{ndf} < 10$.

In this case, we can write the mathematical model for the SER of the MCP-PMT:

$$f_{\text{MCP-PMT}}(Q) = p_0 \Gamma(Q; \alpha, \beta) + (1 - p_0)\text{Tw}_\xi(Q; \alpha', \beta') \tag{3.16}$$

We can get the peak gain $G_p = \alpha/\beta$ and average gain $G_m = p_0\alpha/\beta + (1 - p_0)\delta'_{\text{ts}}\alpha'/\beta'$.

3.2 The timing calibration

3.3 The dark count rate

CHAPTER 4 THE RECONSTRUCTION FOR THE WATER-PHASE

Super-Kamiokande (SK) stands as the world's largest pure water Cherenkov detector, housing 50 kilotons of ultrapure water[48]. Building upon the liquid scintillator-Cherenkov combined track reconstruction technique developed for the MiniBooNE experiment[49], SK collaboration has advanced a likelihood-based reconstruction method, utilizing PMT charge and time information[50], named as fiTQun. For JUNO water-phase, we have implemented targeted improvements to the fiTQun and extended its application to low-energy event reconstruction at the MeV scale.

4.1 The Likelihood function

FiTQun simultaneously determines particle types, vertex positions, momentums, event times. In JUNO water-phase, we just need to determine the vertex position, momentums and event times. The likelihood function of fiTQun is defined as:

$$
\begin{aligned}
\log \mathcal{L}(\boldsymbol{x}; q, t) = & \sum_{j \in \{q=0\}} \log P_j\big(q = 0 \mid \mu_j\big) \\
& + \sum_{i \in \{q>0\}} \log\big(f_{\mathrm{q}}\big(q_i \mid \mu_i\big)\big) \\
& + \sum_{i \in \{q>0\}} \log\big(f_{\mathrm{t}}\big(t_i \mid \boldsymbol{x}\big)\big)
\end{aligned}
\tag{4.1}
$$

- $\boldsymbol{x} = (t_0, x, y, z, p_x, p_y, p_z)$: Event vertex containing time t_0, position (x, y, z), and momentum (p_x, p_y, p_z).
- $\mu_i(\boldsymbol{x})$: Expected PEs at the i-th PMT, computed from the vertex $\boldsymbol{x}$.
- q_i: Charge observed at the i-th PMT, $\{q\}$ is the sequence of q_i, when $q_i = 0$, the PMT is unhitted.
- t_i: Hit time of the i-th PMT, $\{t\}$ is the sequence of t_i.

The first term is the unhit likelihood, which is the probability of no hit in the PMT. The second term is the hit likelihood, which is the probability of detecting hits in the PMT. The third term is the time likelihood, which is the probability of detecting a hit at a certain time.

Since in the operation of the detector, only TQ information (time and charge) is recorded for low-energy events, waveform information is unavailable. At the same time

only the first hit time can be obtained. Therefore, it is necessary to reformulate the likelihood to adopt a first-hit-time-based reconstruction approach. Xuewei Liu et.al developed a first-principles-based reconstruction method using time-charge information or time-PE information in liquid scintillator detectors[51]. We adapt their methodology to reformulate the likelihood function for JUNO water-phase. In low-energy events, where each PMT typically detects only few photon, the number of hits can be directly approximated as NPE (N_{PE}). We can reformulate the likelihood function as Eq. (4.2):

$$
\begin{aligned}
\log \mathcal{L}(\boldsymbol{x}; q, t) = &\sum_{j \in \{q=0\}} \log P_j\big(q = 0 \mid \mu_j\big) + \\
&\sum_{i \in \{q>0\}} \log\big(f_{\mathrm{q}}\big(0 \mid \mu_{i,T_{low}}^{T_i}\big) * f_{\mathrm{t}}(T_i) * f_{\mathrm{q}}(N_{PE,i} - 1 | \mu_{i,T_i}^{T_{up}})\big)
\end{aligned}
\tag{4.2}
$$

In this case, we define the data taking as $[T_{low}, T_{up}]$, and the first hit time of the i-th PMT as T_i, $\mu_{i,T_{low}}^{T_i}$ is the expected PEs in $[T_{low}, T_i]$, same as $\mu_{i,T_i}^{T_{up}}$.

4.2 Response of the water-phase dector

To compute the likelihood, we need to predict how many photons each PMT will detect when given a vertex. The more accurate the predictions are, the better the reconstruction performances. Therefore, we need a comprehensive understanding of the detector response and develop accurate models for it. It naturally comes to mind that when a charged particle enters water, emits Cherenkov photons, and triggers the PMT, this process can be divided into two parts. One pertains to how Cherenkov light is emitted, while the other concerns how the Cherenkov photons propagate and are detected.

4.2.1 The Cherenkov emission profile

When a charged particle travels through a medium at a speed exceeding that of light, it emits Cherenkov photons within a specific solid angle range. The phenomenon arises from local polarization occurring along the charged particle's trajectory: when polarized molecules return to their ground state, they emit electromagnetic radiation. When the refractive index of the medium is n, and the speed of light in vacuum is c_0, the condition of particle speed v_p for Cherenkov emmision is $\beta = v_p/c_0 > 1/n$. When in pure water, whose refractive index is $n_w = 1.333$, and the paitical is electron ($m_0 = 0.511\,\mathrm{MeV}$), the energy threthold is $E_{th} = m_0 \times (\sqrt{1 - 1/n_w^2} - 1) = 0.262\,\mathrm{MeV}$. That means, only when the energy of electron is larger than $0.262\,\mathrm{MeV}$, the Cherenkov photons will emit.

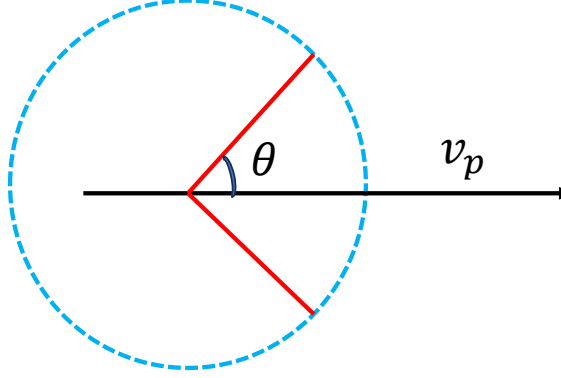The direction of Cherenkov photons can be discribed as: $\cos\theta = \frac{1}{\beta n_w}$ as Fig 4.1 shown.

Figure 4.1   The direction of Cherenkov photons. θ is the angle between the photon emission direction and the direction of particle motion.

When in water, $\cos\theta \approx 0.75$. We can use simulation to get the emmision profile of Cherenkov photons. We used JUNO software (version: J24.2.0) for this simulation. Also, we consider the light yield of Cherenkov by simulating electron with momentum from 2 MeV to 30 MeV. Our simulation is based on JUNO software (JUNOsw)[52], and the version is J24.2.1. We simulated electrons with momenta ranging from 2 to 50 MeV, uniformly distributed within the detector, while their emission directions were randomly oriented.

We extended Dou Wei's angular coordinate definition method for liquid scintillator detectors[53] to Cherenkov radiation detection by incorporating momentum direction degrees of freedom, resulting in the coordinate system illustrated in the figure.

In this simulation, we recorded the angles between the emission directions of all Cherenkov photons and the incident direction of the electron, and we do not care the photons are detected or not. Simultaneously, a crucial parameter is the distance between the photon generation point and the origin position of the charged particle.

- From Fig 4.3, most photons are emitted along the Cherenkov angle ($\cos\theta = 0.75$), while a minority exhibit significant angular deviations from the electron's direction. When calculating the emission angle distribution, it must be analyzed separately for different particle energies rather than applying a single angular distribution to electrons of all energies.

- From Fig 4.4, as the particle moves, Cherenkov photons emitted along the initial segment of its trajectory exhibit a uniform distribution. When the particle's velocity
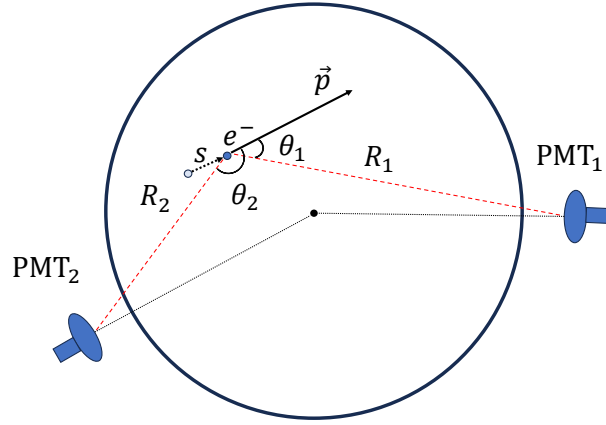
Figure 4.2   Coordinate system definition: θ is the angle of the emission direction of Cherenkov photon and the incident direction of the electron, s is the distance from the position where the particle emits light to its initial position. R is the distance of PMT to the position of electron.

significantly decreases, photon emission drops markedly, with the vast majority of photons being emitted within the first half of the trajectory.
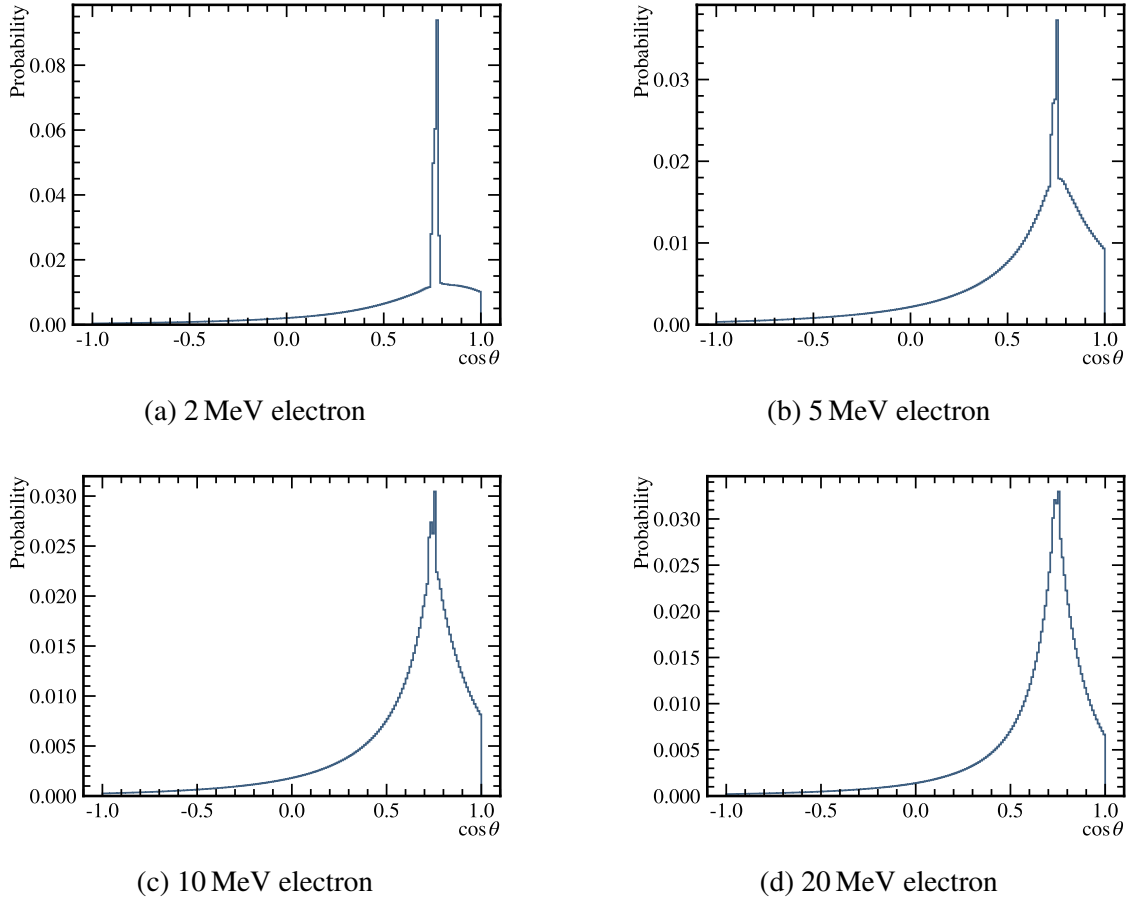
- From Fig 4.5, after traveling some distance, the probability of photons deviating from the Cherenkov angle gradually increases due to multiple scattering. As illustrated in the figure, when electrons undergo multiple scattering, their direction changes significantly, as Fig 4.6 shown. However, when calculating the Cherenkov emission angle, we still use the initial incident direction, thereby producing photons emitted at angles far from the ideal Cherenkov angle.

- In this case, we get the Cherenkov emmision profile ($g(p, s, \theta)$) which describes the proportion of Cherenkov photons emitted at specific locations and directions along the trajectory of a charged particle with a given energy, relative to the total number of emitted photons. For the convenience of research, we use momentum (p) instead of energy (E).

Through Gaussian fitting as shown in Fig 4.7(a) in simulation, we obtain the total number of photons emitted at various energies and calculate the Cherenkov photon yield. After linear fitting, we obtain the relationship between light yield and momentum: $\phi(p) = 1182 \times p - 956$.

4.2.2 The calculation of direct light

After establishing the coordinate system, we can readily determine the number of photons received by a specific PMT when an electron is incident.

$$\mu_{\mathrm{dir}} = \int ds\, g(p, s, \cos\theta)\phi(p)\Omega(R)T(R)\epsilon(\eta) \tag{4.3}$$

(a) 2 MeV electron

(b) 5 MeV electron

(c) 10 MeV electron

(d) 20 MeV electron

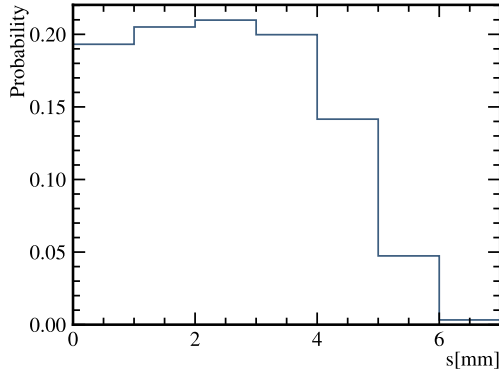Figure 4.3   The relationship of emission probability with $\cos\theta$.

- R is the distance between the position of electron and the PMT.
- $\Omega(R)$ is the solid angle factor of PMT.
- $T(R)$ is the light transmission factor.
- $\epsilon(\eta)$ is the PMT angular acceptance of PMT, and η is the incident angle of light when captured by PMT.

4.2.2.1 The solid angle factor

The main PMTs employed in JUNO are 20-inch with a radius of $a = SI0.622m$. And we can calculate the solid angle of PMT by Eq. (4.4).

$$\Omega(R) = \frac{\pi a^2}{4\pi(R^2 + a^2)} \times (4\pi) = \frac{\pi a^2}{R^2 + a^2} \tag{4.4}$$

This approximation remains valid only when PMTs are sufficiently distant from the particle. In JUNO, PMTs are mounted at around 19.5 m , while our region of interest lies within 17.7 m. Based on SK's experience, the approximation holds effectively at radial distances $R > 1.5$ m.
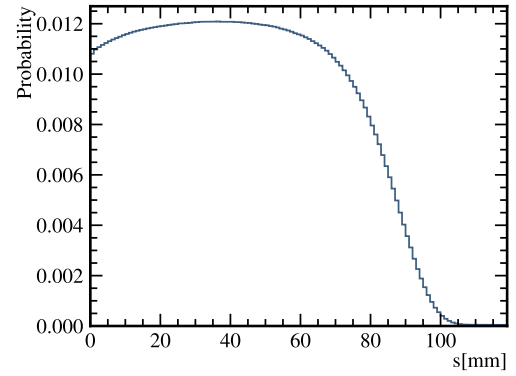
(a) 2 MeV electron
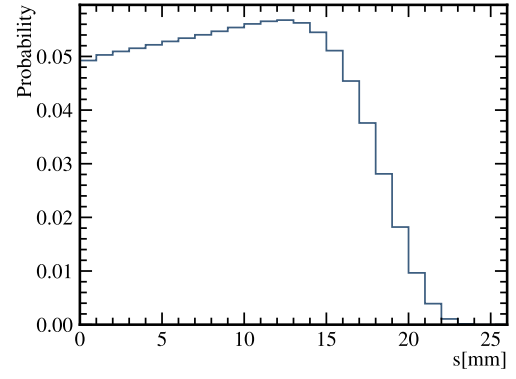
(b) 5 MeV electron
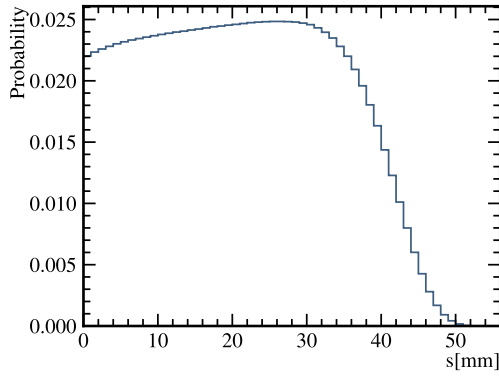
(c) 10 MeV electron

(d) 20 MeV electron

Figure 4.4　The relationship of emission probability with s.

4.2.2.2 The transmission factor

In our work, we just use Eq. (4.5), and the attenuation length L^a is 75 m.

$$T(R) = \exp(-R/L^a) \tag{4.5}$$

4.2.2.3 PMT angular accptance

4.3 The Fast reconstruction (FRE) of the JUNO water-phase
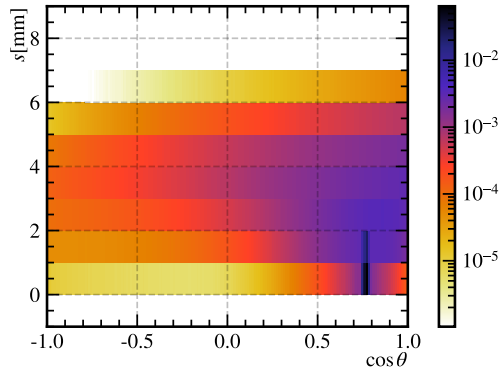
4.4 The evaluation of reconstructions

4.4.1 The parameters used in the reconstruction

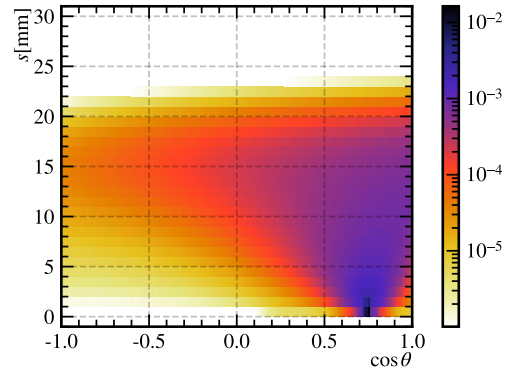## 4.4.2 The reconstruction goodness of reconstruction

The goodness of vertex is defined

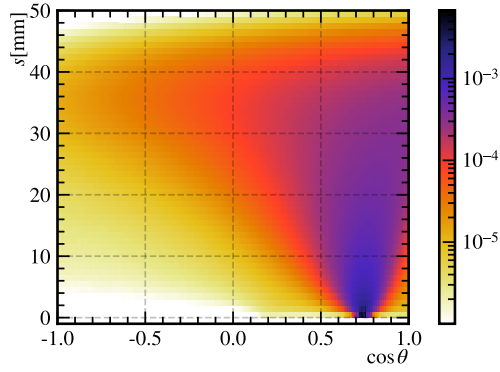## 4.4.3 In the dector simulation

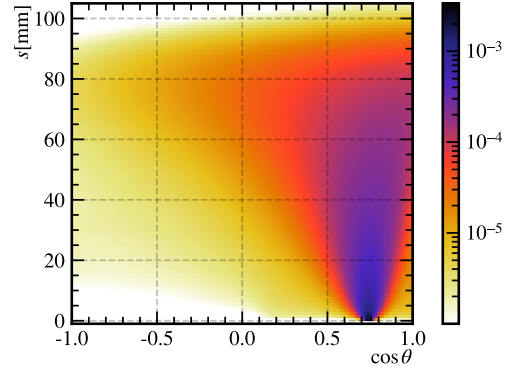## 4.4.4 In the electronic simulation

(a) 2 MeV electron

(b) 5 MeV electron

(c) 10 MeV electron

(d) 20 MeV electron

Figure 4.5　The relationship of emission probability with s and $\cos\theta$.
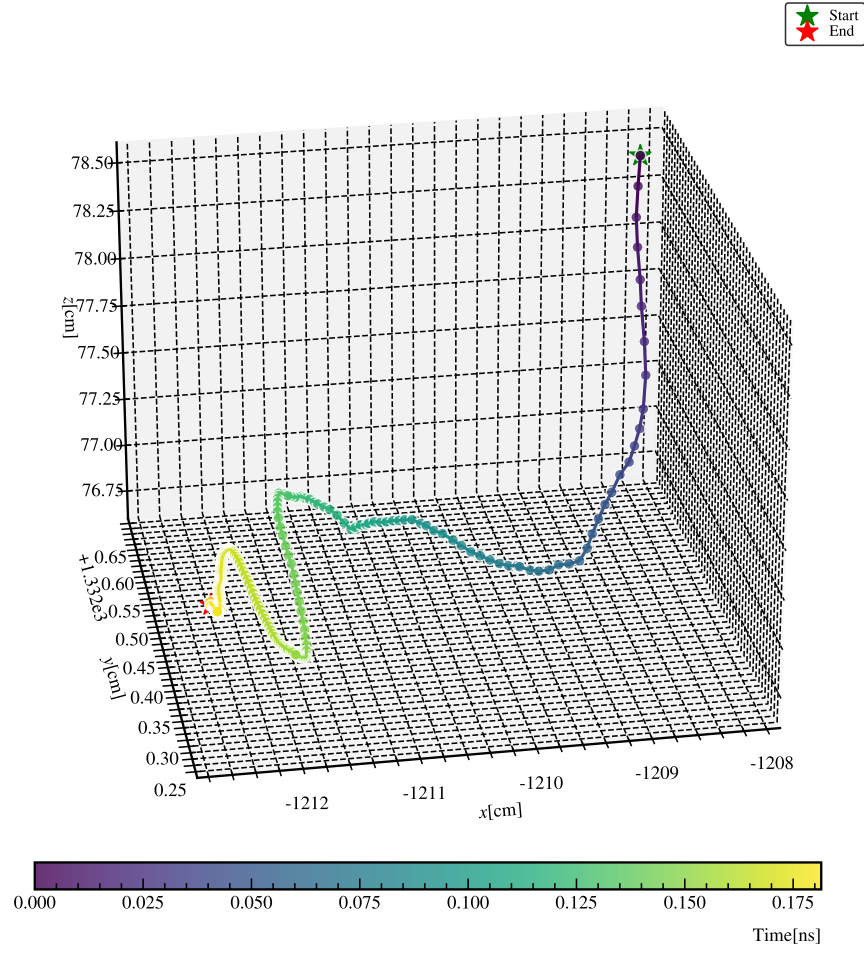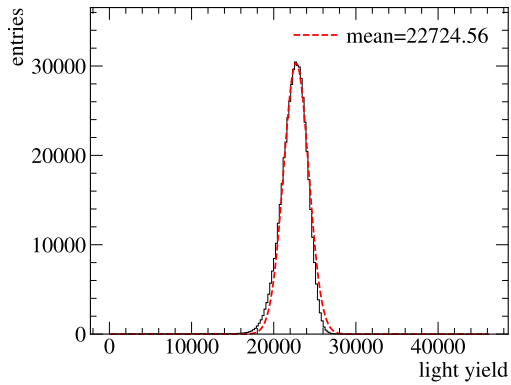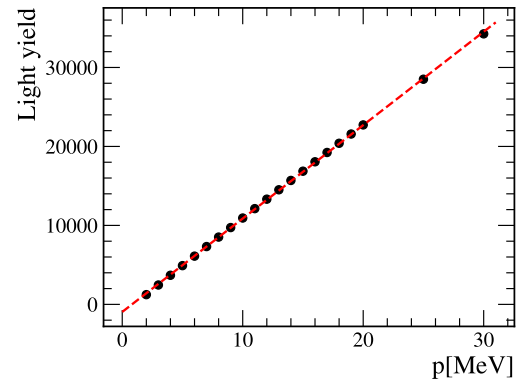
Figure 4.6　An example of a 10 MeV electron undergoing multiple scattering.

(a) An example of Gaussian fit for light yield.

(b) 5 MeV electron

Figure 4.7　The relationship of emission probability with *s* and .

REFERENCES

[1]   Breitenberger E. Scintillation spectrometer statistics[J]. Progress in nuclear physics, 1955, 4: 56-94.

[2]   Chen L, et al. Optimization of the electron collection efficiency of a large area MCP-PMT for the JUNO experiment[J/OL]. Nucl. Instrum. Meth. A, 2016, 827: 124-130. https://www.scie ncedirect.com/science/article/pii/S0168900216303308. DOI: https://doi.org/10.1016/j.nima.2 016.04.100.

[3]   Bellamy E, et al. Absolute calibration and monitoring of a spectrometric channel using a photo-multiplier[J/OL]. Nucl. Instrum. Meth. A, 1994, 339(3): 468-476. https://www.sciencedirect. com/science/article/pii/016890029490183X. DOI: https://doi.org/10.1016/0168-9002(94)901 83-X.

[4]   Tao S X, et al. Secondary electron emission materials for transmission dynodes in novel photo-multipliers: A review[J]. Materials, 2016, 9(12): 1017.

[5]   Furman M, Pivi M. Probabilistic model for the simulation of secondary electron emission[J]. Physical review special topics-accelerators and beams, 2002, 5(12): 124404.

[6]   Bruining H, De Boer J. Secondary electron emission: Part I. Secondary electron emission of metals[J]. Physica, 1938, 5(1): 17-30.

[7]   Ushio Y, et al. Secondary electron emission studies on MgO films[J]. Thin Solid Films, 1988, 167(1-2): 299-308.

[8]   Jokela S J, et al. Secondary Electron Yield of Emissive Materials for Large-Area Micro-Channel Plate Detectors: Surface Composition and Film Thickness Dependencies[J]. Physics Procedia, 2012, 37: 740-747.

[9]   Olano L, Montero I. Energy spectra of secondary electrons in dielectric materials by charging analysis[J/OL]. Results in Physics, 2020, 19: 103456. https://www.sciencedirect.com/science/ article/pii/S2211379720319173. DOI: https://doi.org/10.1016/j.rinp.2020.103456.

[10]   Mane A U, et al. An Atomic Layer Deposition Method to Fabricate Economical and Robust Large Area Microchannel Plates for Photodetectors[J]. Physics Procedia, 2012, 37: 722-732.

[11]   Guo L, et al. Effects of secondary electron emission yield properties on gain and timing perfor-mance of ALD-coated MCP[J]. Nucl. Instrum. Meth. A, 2021, 1005: 165369.

[12]   Nathan R, Mee C. The energy distribution of photoelectrons from the K2CsSb photocathode [J/OL]. physica status solidi (a), 1970, 2(1): 67-72. https://api.semanticscholar.org/CorpusID: 97164824.

[13]   Zhang A, et al. Performance evaluation of the 8-inch MCP-PMT for Jinping Neutrino Experi-ment[J/OL]. Nucl. Instrum. Meth. A, 2023, 1055: 168506. DOI: 10.1016/j.nima.2023.168506.

[14]   Zhu Y, et al. The mass production and batch test result of 20" MCP-PMTs[J/OL]. Nucl. Instrum. Meth. A, 2020, 952: 162002. https://www.sciencedirect.com/science/article/pii/S016890021 9303833. DOI: https://doi.org/10.1016/j.nima.2019.03.057.

REFERENCES

[15] Matsuoka K. Development and production of the MCP-PMT for the Belle II TOP counter[J/OL]. Nucl. Instrum. Meth. A, 2014, 766: 148-151. https://www.sciencedirect.com/science/article/pii/S0168900214005026. DOI: https://doi.org/10.1016/j.nima.2014.05.003.

[16] Krauss S, et al. Performance of the most recent Microchannel-Plate PMTs for the PANDA DIRC detectors at FAIR[J/OL]. Nucl. Instrum. Meth. A, 2023, 1057: 168659. https://www.sciencedirect.com/science/article/pii/S0168900223006496. DOI: https://doi.org/10.1016/j.nima.2023.168659.

[17] Cao Z, et al. Upgrading Plan Towards Multi-messenger Observation with LHAASO[J/OL]. EPJ Web of Conferences, 2019. https://api.semanticscholar.org/CorpusID:181399433.

[18] Kishimoto N, et al. Lifetime of MCP-PMT[J/OL]. Nucl. Instrum. Meth. A, 2006, 564(1): 204-211. https://www.sciencedirect.com/science/article/pii/S0168900206006991. DOI: https://doi.org/10.1016/j.nima.2006.04.089.

[19] Lehmann A, et al. Latest Technological Advances with MCP-PMTs[J]. J. Phys.: Conf. Ser., 2022, 2374(1): 012128.

[20] Cao W, et al. Secondary electron emission characteristics of the Al2O3/MgO double-layer structure prepared by atomic layer deposition[J/OL]. Ceramics International, 2021, 47(7): 9866-9872. DOI: 10.1016/j.ceramint.2020.12.128.

[21] Zhang Z, et al. Effect of Al2O3/MgO Composite Layer on the Properties of Microchannel Plate [J]. Surface Technology, 2021, 50(6): 199-205.

[22] Abusleme A, et al. Mass testing and characterization of 20-inch PMTs for JUNO[J]. The European Physical Journal C, 2022, 82(12): 1168.

[23] Orlov D, et al. High collection efficiency MCPs for photon counting detectors[J/OL]. JINST, 2018, 13(01): C01047. DOI: 10.1088/1748-0221/13/01/C01047.

[24] Zhang H, et al. Gain and charge response of 20" MCP and dynode PMTs[J]. JINST, 2021, 16 (08): T08009.

[25] Yang Y, et al. MCP performance improvement using alumina thin film[J]. Nucl. Instrum. Meth. A, 2017, 868: 43-47.

[26] Tan H H. A statistical model of the photomultiplier gain process with applications to optical pulse detection[J/OL]. The Telecommunications and Data Acquisition Report, 1982. http://hdl.handle.net/10150/612894.

[27] Bartlett M S, Harris T E. The Theory of Branching Processes[M/OL]. Springer Berlin, 1963. https://api.semanticscholar.org/CorpusID:90485223.

[28] Woodward P M. A statistical theory of cascade multiplication[J/OL]. Mathematical Proceedings of the Cambridge Philosophical Society, 1948, 44(3): 404-412. DOI: 10.1017/S0305004100024403.

[29] Prescott J. A statistical model for photomultiplier single-electron statistics[J]. Nuclear Instruments and Methods, 1966, 39(1): 173-179.

[30] Kalousis L. Calibration of the Double Chooz detector and cosmic background studies[D]. University of Strasbourg, 2012.

[31] Kalousis L, et al. A fast numerical method for photomultiplier tube calibration[J]. JINST, 2020, 15(03): P03023.

[32] Bruining H. Physics and applications of secondary electron emission[M]. Pergamon Press, 1954.

[33] Baroody E. A theory of secondary electron emission from metals[J]. Physical Review, 1950, 78(6): 780.

[34] Dekker A, Van der Ziel A. Theory of the production of secondary electrons in solids[J]. Physical Review, 1952, 86(5): 755.

[35] Wolff P A. Theory of secondary electron cascade in metals[J/OL]. Phys. Rev., 1954, 95: 56-66. https://link.aps.org/doi/10.1103/PhysRev.95.56.

[36] Kanaya K, et al. Secondary electron emission from insulators[J/OL]. J. Phys. D: Appl. Phys., 1978, 11(17): 2425. https://dx.doi.org/10.1088/0022-3727/11/17/015.

[37] Vaughan J. A new formula for secondary emission yield[J/OL]. IEEE Transactions on Electron Devices, 1989, 36(9): 1963-1967. DOI: 10.1109/16.34278.

[38] Luo F J, et al. Design & Optimization of the HV divider for JUNO 20-inch PMT[A]. 2023.

[39] Nelson, Rick. High-Definition Oscilloscopes Optimize Vertical Resolution[J/OL]. EE-Evaluation Engineering Online, 2016[Aug. 31, 2016]. https://www.electronicdesign.com/technologies/test-measurement/article/21206728/high-definition-oscilloscopes-optimize-vertical-resolution.

[40] Xu D, et al. Towards the ultimate PMT waveform analysis for neutrino and dark matter experiments[J/OL]. JINST, 2022, 17(06): P06040. https://dx.doi.org/10.1088/1748-0221/17/06/P06040.

[41] Wang Y, et al. The Fast Stochastic Matching Pursuit for Neutrino and Dark Matter Experiments [A]. 2024. arXiv: 2403.03156.

[42] Gagunashvili N D. Comparison of weighted and unweighted histograms[J]. Statistics, 2012: 43-44.

[43] Gelman A, Hill J. Analytical methods for social research: Data Analysis Using Regression and Multilevel/Hierarchical Models[M]. Cambridge University Press, 2006.

[44] Cowan G. Statistical Data Analysis[M]. Illustrated edition ed. Oxford: New York: Oxford University Press, 1997.

[45] Chen P, et al. Photoelectron backscattering in the microchannel plate photomultiplier tube[J]. Nucl. Instrum. Meth. A, 2018, 912: 112-114.

[46] Beck A H. Physical Electronics: Handbook of Vacuum Physics[M]. Elsevier, 1966.

[47] Jorgensen B. The Theory of Dispersion Models[M/OL]. Taylor & Francis, 1997. https://books.google.co.jp/books?id=0gO7bgs_eSYC.

[48] Fukuda S, Y. Fukuda E I, T. Hayakawa, et al. The Super-Kamiokande detector[J/OL]. Nuclear Instruments and Methods in Physics Research Section A: Accelerators, Spectrometers, Detectors and Associated Equipment, 2003, 501(2): 418-462. https://www.sciencedirect.com/science/article/pii/S016890020300425X. DOI: https://doi.org/10.1016/S0168-9002(03)00425-X.

REFERENCES

[49] Patterson R, Laird E, Liu Y, et al. The extended-track event reconstruction for MiniBooNE [J/OL]. Nuclear Instruments and Methods in Physics Research Section A: Accelerators, Spectrometers, Detectors and Associated Equipment, 2009, 608(1): 206-224. https://www.scienced irect.com/science/article/pii/S0168900209012480. DOI: https://doi.org/10.1016/j.nima.2009. 06.064.

[50] Jiang M, Abe K, Bronner, et al. Atmospheric neutrino oscillation analysis with improved event reconstruction in super-kamiokande iv[J/OL]. Progress of Theoretical and Experimental Physics, 2019, 2019(5): 053F01. https://doi.org/10.1093/ptep/ptz015.

[51] Liu X, Dou W, Xu B, et al. First-principle event reconstruction by time-charge readouts for TAO [J/OL]. Eur. Phys. J. C, 2025, 85(4): 438. DOI: 10.1140/epjc/s10052-025-14161-6.

[52] Yu P, et al. Multi-threaded Simulation Software for the JUNO Experiment[A]. 2025. arXiv: 2503.20219.

[53] Dou W, Xu B, Zhou J, et al. Reconstruction of point events in liquid-scintillator detectors subjected to total internal reflection[J/OL]. Nucl. Instrum. Meth. A, 2023, 1057: 168692. DOI: 10.1016/j.nima.2023.168692.